nature sustainability

Article

https://doi.org/10.1038/s41893-022-00974-w

Polymeric membranes with aligned zeolite nanosheets for sustainable energy storage

Received: 2 March 2022

Accepted: 6 September 2022

Yongsheng Xia[1], Hongyan Cao[1], Fang Xu[2], Yuxin Chen[2], Yu Xia[1], Dezhu Zhang[1], Liheng Dai[2], Kai Qu[2], Cheng Lian[2], Kang Huang[1] ✉, Weihong Xing[1], Wanqin Jin[1] ✉ and Zhi Xu[2] ✉

Membrane technologies with low environmental impacts and ease of use have a wide spectrum of applications, with the potential to provide more sustainable solutions in domains such as water, energy and pollution treatment. However, the design of membranes is subject to a trade-off between ion conductivity and selectivity. Here we show a composite polymeric membrane that breaks this dilemma and supports both high proton conductivity (80.1 mS cm^{-1}) and good vanadium ion selectivity (2.01×10^5 S min cm^{-3}). Underlying this synthetic success is a flow-processing technique through which zeolite nanosheet fillers are oriented in a preferred direction throughout a polymer Nafion matrix. As a result, pairing this aligned membrane with a vanadium flow battery leads to a high energy efficiency of >80% at 200 mA cm^{-2} and remarkable stability over 1,000 cycles. This work enables the design of membranes that combine otherwise mutually exclusively properties for many possible applications beyond energy storage.

Renewable energy is poised to account for an increasing share of the future power portfolio to address sustainability challenges that have resulted from massive carbon emissions from fossil fuels. The ever-growing urgency to accelerate decarbonization of the economy is driving the development and adoption of large-scale energy storage and conversion technologies, such as flow batteries (FBs)[1–3], fuel cells[4,5] and water electrolysers[6,7], to tackle the intermittency and instability of renewable energy. Ion-selective membranes are the central component in many electrochemical devices and govern the efficiency of energy conversion and utilization. In aqueous FBs with recyclable non-combustible electrolytes, ion-selective membranes conduct ions to complete an electric circuit and separate chemical reactions between the anode and cathode[8]. However, current membrane materials, including commonly used perfluorosulfonic acid-based Nafion, generally suffer from low ion selectivity and limited conductivity due to their irregular channels and serious swelling[9]. The design and development of high-efficiency membranes are beneficial for maximizing renewable energy utilization and promoting energy sustainability[10–12].

To devise ion-selective membranes, there are two major considerations. One is to fabricate fast and regular ion-transport channels with precise selectivity[13–16], and the other is to construct membrane with highly aligned and oriented channel architecture[17,18]. Molecular sieve materials, such as zeolites, with well-defined interconnected rigid channels and super-stable frameworks are prospective materials[19]. Oriented zeolite polycrystalline membranes have initially presented potential for efficient ion separation[20], while their preparation and application techniques still pose great challenges owing to grain boundary defects, incomplete/interlaced coverage, random misoriented intergrowth and fragile structural characteristics[21–23].

An alternative approach is to incorporate zeolite into the polymer matrix, which could take advantage of the molecular sieves and feasible fabrication processes used for pure polymer membranes[24–26]. However, it is worth noting that the isotropy of traditional zeolite materials makes it impossible to align their molecular sieving channels in polymers. Two-dimensional (2D) zeolite nanosheets (ZNs)[20,23,27] provide a convenient and practical route to achieve this purpose[28]. The value

---

[1]State Key Laboratory of Materials-Oriented Chemical Engineering, Nanjing Tech University, Nanjing, China. [2]State Key Laboratory of Chemical Engineering, East China University of Science and Technology, Shanghai, China. ✉e-mail: kanghuang@njtech.edu.cn; wqjin@njtech.edu.cn; zhixu@ecust.edu.cn

behind ordered, in-plane nanosheets within polymers is apparent, as these additions help maximize the benefits of the high-aspect-ratio structures[29]. In particular, this merit will be further magnified by adopting 2D materials with intrinsically regular sieving channels. However, owing to entropy, the distribution of nanosheets in polymers gravitates towards randomness, making it challenging to develop composite membranes with highly aligned architectures.

Here, we show a simple and controllable volatilizing shear flow-induced alignment (VSFI) approach to disperse aluminiferous ZNs in the polymeric matrix in an ordered way (Fig. 1a and Supplementary Fig. 1). The shear force generated during volatilization serves to control the orientation of the ZNs in the polymer. These aligned nanosheets could both maximize discrimination of ions and enable fast proton transport, therefore breaking the trade-off between ion selectivity and conductivity, together with enhanced tensile strength and swelling resistance. The favourable combination of conductivity and selectivity in the aligned membrane is further manifested in flow batteries that show high energy efficiency of >80% and impressive stability over 1,000 cycles. This work provides an effective strategy for the rational design of membranes for applications, including safe, eco-friendly and high-performance flow battery systems for sustainable large-scale energy storage.

Results

Membrane fabrication

First, high-aspect-ratio aluminiferous ZNs with an optimized Si/Al ratio of 23.7 ± 1.7 were synthesized via a modified MFI-type silicalite ZN synthesis approach[20,23] (see Methods and Supplementary Note 1 for details, and Supplementary Figs. 2–4). The ZNs presented a classic rhombus morphology with an edge thickness of 7.5 nm and a lateral dimension of $4.9 \times 2.7\ \mu m^2$ (Fig. 1b and Supplementary Fig. 5), and exhibited excellent chemical and thermal stability (Supplementary Figs. 6 and 7). Additionally, the aluminiferous ZN showed nearly cylindrical *b* axis straight channels along the thickness (Fig. 1c and Supplementary Figs. 8–10) with a special hydrophilic ionic surface (see Supplementary Fig. 11 and Supplementary Note 2 for details).

We found that local shear flow could effectively induce the alignment of high-aspect-ratio nanofillers in the suspending fluid during material processing, especially in polymer processing[30,31]. In this study, the volatilization process in the VSFI method provided a controllable local shear flow to facilitate the uniform and ordered distribution of ZNs in the polymeric phase (Fig. 1d). A homogeneous Nafion hybrid casting solution with well-dispersed ZNs (Supplementary Fig. 12) was utilized to demonstrate the feasibility of our VSFI strategy. Initially, ZNs were randomly distributed in the casting solution without a specific orientation (Fig. 1e, panel i). Following the volatilization of the solvent, shear flow was generated by the liquid supplement to volatilization. The difference in the shear flow around the ZNs caused a gradual decrease in the angle (θ) between the nanosheet and the plane direction (Fig. 1e, panel ii). With appropriate choices of volatilization temperature and pressure, the nanosheets arranged in a highly oriented in-plane manner and were uniformly distributed in the polymer (Fig. 1e, panel iii). To understand the volatilizing shear flow-induced alignment process, we used computational fluid dynamics to analyse the shear flow rate distribution around the ZN during the volatilization process. According to the Newtonian law of viscosity, the volatilizing shear flow resulted in an efficient shear flow force, τ ($\tau = \mu\, du/dy$, where μ is the viscosity and du/dy is the shear flow rate). As shown in Fig. 1f, there was an obvious shear force gradient field along the ZN, and the shear force at the two end points of the ZN presented different distributions, which acted on the angle adjustment and alignment of the ZNs.

The aligned composite membranes were characterized by scanning electron microscopy (SEM) and transmission electron microscopy (TEM). A series of random cross-sectional SEM images revealed that all the ZNs were almost parallel to the membrane surface and evenly distributed in the polymer (Supplementary Figs. 13 and 14), rather than accidental events. The TEM images and energy dispersive X-ray spectroscopy (EDS) results (Fig. 2a,b) also proved the aligned nature of the ZNs in the polymeric matrix. To further verify the orderliness of the nanosheets, wide-angle X-ray scattering (WAXS) measurements were employed to quantitatively analyse the orientation degree of the ZNs in the polymer. As shown in Fig. 2c, the aligned composite membrane showed a typical aeolotropic scattering pattern, indicating the aligned state of the ZNs in the polymer. A sharp peak at $\varphi = 90°$ is observed in the corresponding azimuthal angle (φ) plot. The calculated orientation degree, identified by the Herman's orientation factor (*f*; Methods), was as high as 0.81, further proving that ZNs were well assembled in the membrane[32].

The internal structure of the aligned composite membrane was studied in detail using focused ion beam-scanning electron microscopy (FIB-SEM). A protective Pt layer was deposited on the upper surface of the membrane before analysis, and then an FIB was applied to carve a trench and mill a series of continuous thin slices (Fig. 2d). The corresponding cross-sectional SEM images were recorded. Figure 2e shows a representative cross-sectional SEM image exposed on FIB milling of the membrane. A 3D model (Fig. 2f) was reconstructed on the basis of the SEM images. By segmenting different phases, the ZNs were clearly presented in a surface-rendered view (Fig. 2g). It can be observed that the ZNs in the polymeric phase were uniformly distributed in parallel, which was consistent with the WAXS results. The orientation degree of the ZNs in the membrane was also quantified by analysing the FIB-SEM tomograms, and the statistical orientation histogram showed a preferred orientation of nanosheets at an angle close to 0°, parallel to the membrane surface (Fig. 2h). The corresponding pie chart of the angle distribution percentage (Fig. 2i and Supplementary Table 1) further revealed that more than 80% of the nanosheets were oriented at angles between 0° and 10°. This preferential orientation of ZNs deviates highly from the random orientation, which could provide an effective barrier to resist the transport of unwelcome ions and maximize the ion-sieving capability of the membranes.

The local shear flow force generated by the volatilization process is highly responsible for the uniform alignment of the nanosheets in the polymer. Selecting a suitable volatilization rate (υ) is crucial for a membrane with a high degree of orientation. Generally, when the casting solution composition is unchanged, υ can be easily adjusted by rationally setting the volatilization temperature (T) and absolute pressure (P). Figure 3a shows an experimental correlation relating the actual υ to both T and P, which determined the quality of the membranes (Fig. 3b and Supplementary Fig. 15). When υ was less than $0.18\ g\ cm^{-2}\ h^{-1}$, ZNs could not uniformly distribute in polymer and were almost deposited at the bottom of the composite, while cracked and brittle membranes were obtained owing to a dearth of crystallinity. However, excessive υ resulted in discontinuous membranes with obvious bubble defects. Our experimental results indicated that the optimal υ range was $0.43 \pm 0.05\ g\ cm^{-2}\ h^{-1}$, where the corresponding *f* of the membranes was located at a high level of more than 0.7 (Fig. 3c). When υ deviated from the best interval, the distribution of ZNs in the polymer moved towards disorder, leading to a low *f*. Figure 3d shows an intuitive comparison of composite membranes with different *f* of 0.81 and 0.46. Compared with the highly aligned composite membrane, ZNs were distributed randomly in the low-aligned composite membrane without preferred orientation (Fig. 3d and Supplementary Fig. 16). The VSFI method was further confirmed by preparing a series of highly aligned membranes under the optimal υ, but using different T and P parameters (Fig. 3e). Moreover, we also fabricated a highly aligned ZN membrane with different ZN contents (2–4 wt%) via the VSFI method (Fig. 3f).

Membrane properties

A membrane with high ion selectivity and conductivity is very important for FBs. To reveal the effects of alignment on the membrane properties,

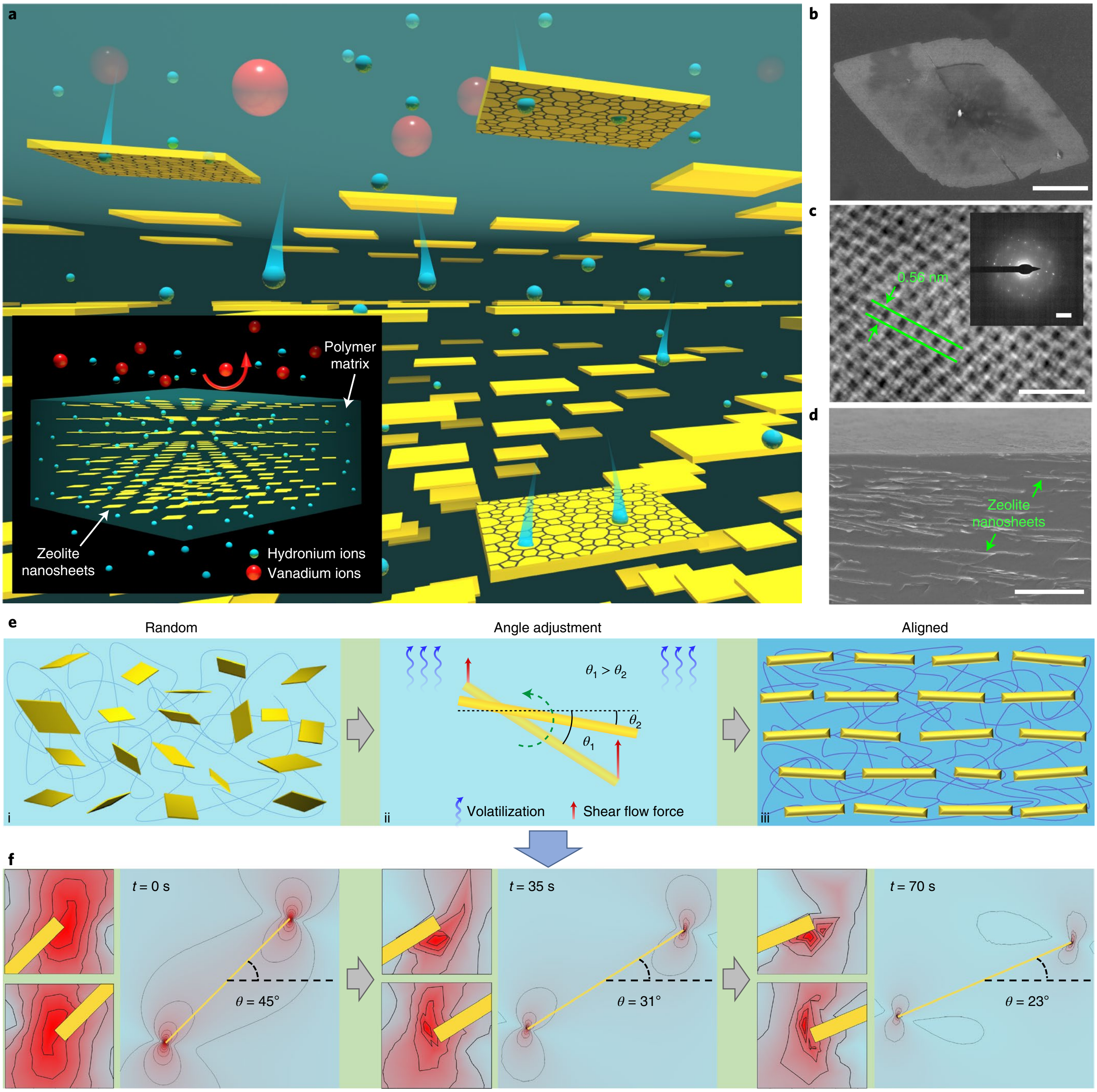

Fig. 1 | Structure and formation process schematics of aligned zeolite nanosheets in a polymer membrane. a, Schematic of the internal perspective and the global perspective (inset) of a composite membrane with aligned ZNs for ion-selective transport. **b**, The SEM image of the ZN. **c**, The integrated differential phase contrast scanning transmission electron microscopy image of the ZN. The inset in **c** is the corresponding [010] (*b* axis along the thickness direction) zone axis electron diffraction pattern from the ZN. **d**, Cross-sectional SEM image of the aligned ZN composite membrane. **e**, Schematic of the formation process of the aligned ZN composite membrane: (i) randomly dispersed ZNs in casting solution; (ii) angle adjustment of ZN under shear flow force; and (iii) aligned distribution of ZNs in polymer membrane. The filaments in **e** represent disordered polymer chains. **f**, Computational fluid dynamics analysis of the ZN alignment process. The red region represents a higher shear force than the cyan region. Scale bars, 1 μm (**b**); 5 nm (**c**), 2 nm^{-1} (**c**, inset); 5 μm (**d**).

highly aligned composite membranes, with *f* of approximately 0.8 (abbreviated as h-ZN), and low-aligned composite membranes, with *f* of approximately 0.45 (abbreviated as l-ZN), were used to investigate the ion permeation rate and conductivity. In addition, to highlight the superiority of high-aspect-ratio nanosheets, pure Nafion membranes (abbreviated as p-Nf; Supplementary Fig. 17) and isotropic (bulk-type) zeolite counterpart incorporated membranes with *f* of less than 0.05 (abbreviated as i-ZB; Supplementary Fig. 18) were also prepared under the same conditions as h-ZN. All composite membranes involved in this study were controlled at the same optimal doping amount of 3 wt% and with a thickness of ~46 μm, unless otherwise specified (Supplementary Fig. 19 and Supplementary Note 3).

Taking the vanadium flow battery (VFB) as an example, the resistance to vanadium ions was investigated next. As shown in Fig. 4a and Supplementary Fig. 20, once zeolites were incorporated into the polymeric phase, all the membranes exhibited enhanced resistance to

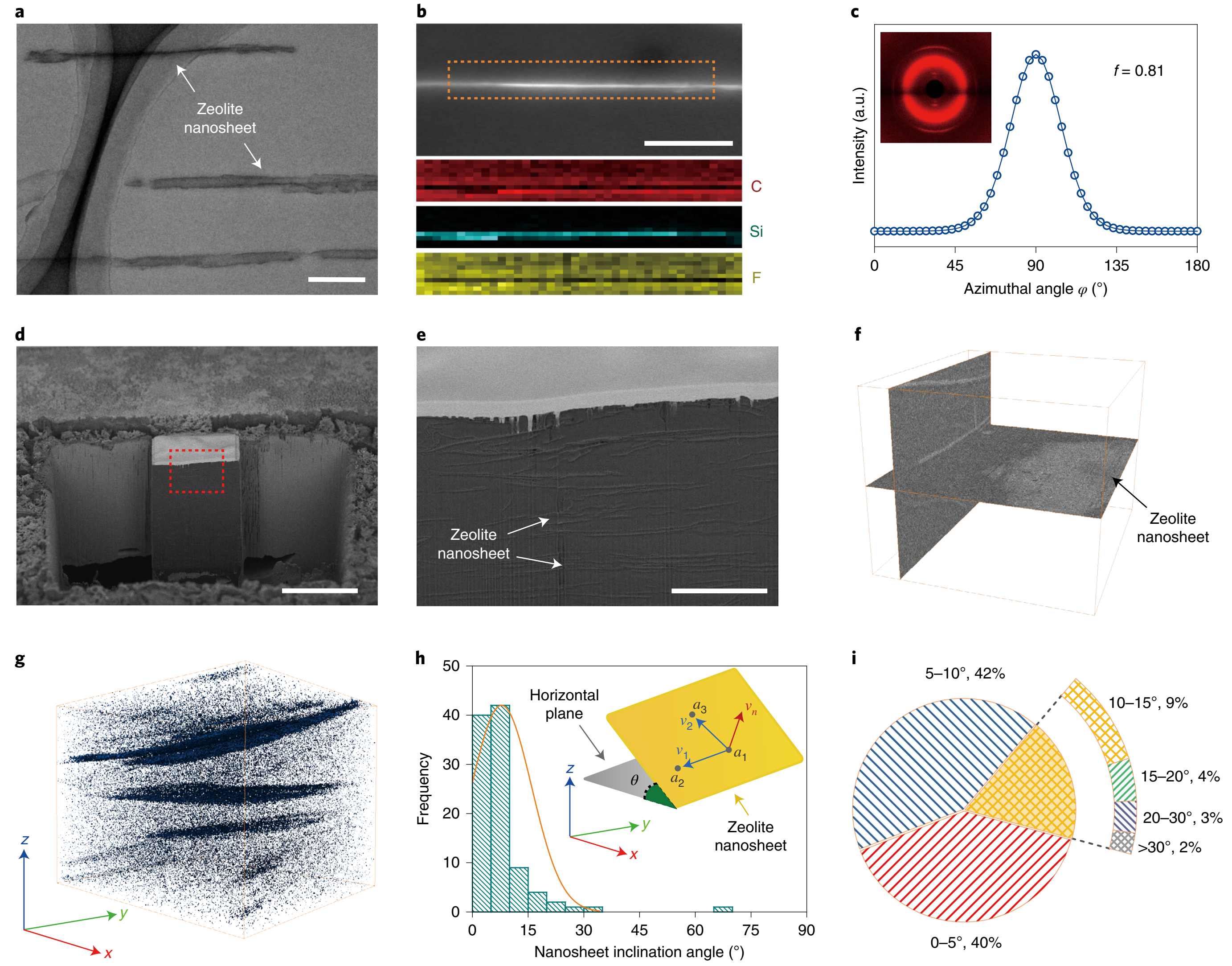

Fig. 2 | Structure characterizations of polymer membrane featuring aligned ZNs. a,**b**, TEM image (**a**) and EDS results (**b**). **c**, 2D WAXS image and azimuthal angle plots. **d**, The overview SEM image of the trench on the membrane surface. The region marked by the red dashed frame in the cross-sectional image was selected for further analysis. **e**, Representative cross-sectional SEM image during the FIB milling. **f**, Orthogonal cross-sections through the 3D reconstructed FIB-SEM tomogram. Nanosheets appear as a bright pattern on the light grey polymer matrix, and the high-aspect-ratio nanosheet lying on a plane parallel to the membrane surface is visible intuitively. **g**, Surface-rendered view of the segmented FIB-SEM tomograms. Nanosheets are shown in dark blue. **h**,**i**, Statistical orientation histogram (**h**) and corresponding pie chart (**i**) of the angle (*θ*) between the nanosheet and the membrane surface. Scale bars, 500 nm (**a**); 100 nm (**b**); 20 μm (**d**); 5 μm (**e**).

vanadium ions compared with p-Nf, owing to the absolute vanadium ion-sieving ability of the zeolite rigid channels (Fig. 1c and Supplementary Figs. 21 and 22). Benefiting from the unique 2D structure, the use of ZNs as fillers resulted in higher increases in the vanadium resistance than that of bulk-type zeolite counterparts, strongly proving the superiority of nanosheet materials. Among them, h-ZN exhibited the lowest vanadium ion permeability, indicating that the higher alignment of ZNs indeed contributes to the better barrier effect for larger size activities in FBs. Furthermore, as shown in Fig. 4b, the vanadium permeability measured in the experiment was highly consistent with the calculated theoretical prediction based on the Bharadwaj model[33] considering the effect of *f*, further verifying the superiority of the orderly alignment.

Electrochemical impedance spectrum testing showed that the introduction of zeolites apparently decreased the area resistance of the membranes (Supplementary Figs. 23 and 24), and the proton conductivity also corresponded well with the tendency of the resistance to vanadium ions (Fig. 4a), following the order of h-ZN > l-ZN > i-ZB > p-Nf. Among these, h-ZN possessed the strongest proton conductivity (80.1 mS cm^{-1}), which was 2.6 times higher than that of p-Nf (31.1 mS cm^{-1}) and 1.9 times higher than that of commercial Nafion 212 (Nf 212) (41.5 mS cm^{-1}) (Supplementary Fig. 25). On the basis of the above results, h-ZN exhibited the highest vanadium ion selectivity (20.1×10^4 S min cm^{-3}), usually identified as the ratio of the proton conductivity to the vanadium ion permeability in a VFB, which was 8.4 times higher than that of p-Nf (2.4×10^4 S min cm^{-3}) and 2.8 times higher than that of Nf 212 (7.1×10^4 S min cm^{-3}) (Supplementary Fig. 25). It is worth noting that the vanadium ion selectivity of h-ZN increased by more than 50% compared to that of l-ZN. All these results demonstrated that the preferential orientation of ZNs in the polymer (Fig. 4c) resulted in a sieving effect of the high-aspect-ratio nanosheets close to maximum and effectively promoted the transport of protons as quickly as possible.

We reasoned that the fast proton transport behaviour was not only derived from the structural variations within the polymer[34,35]

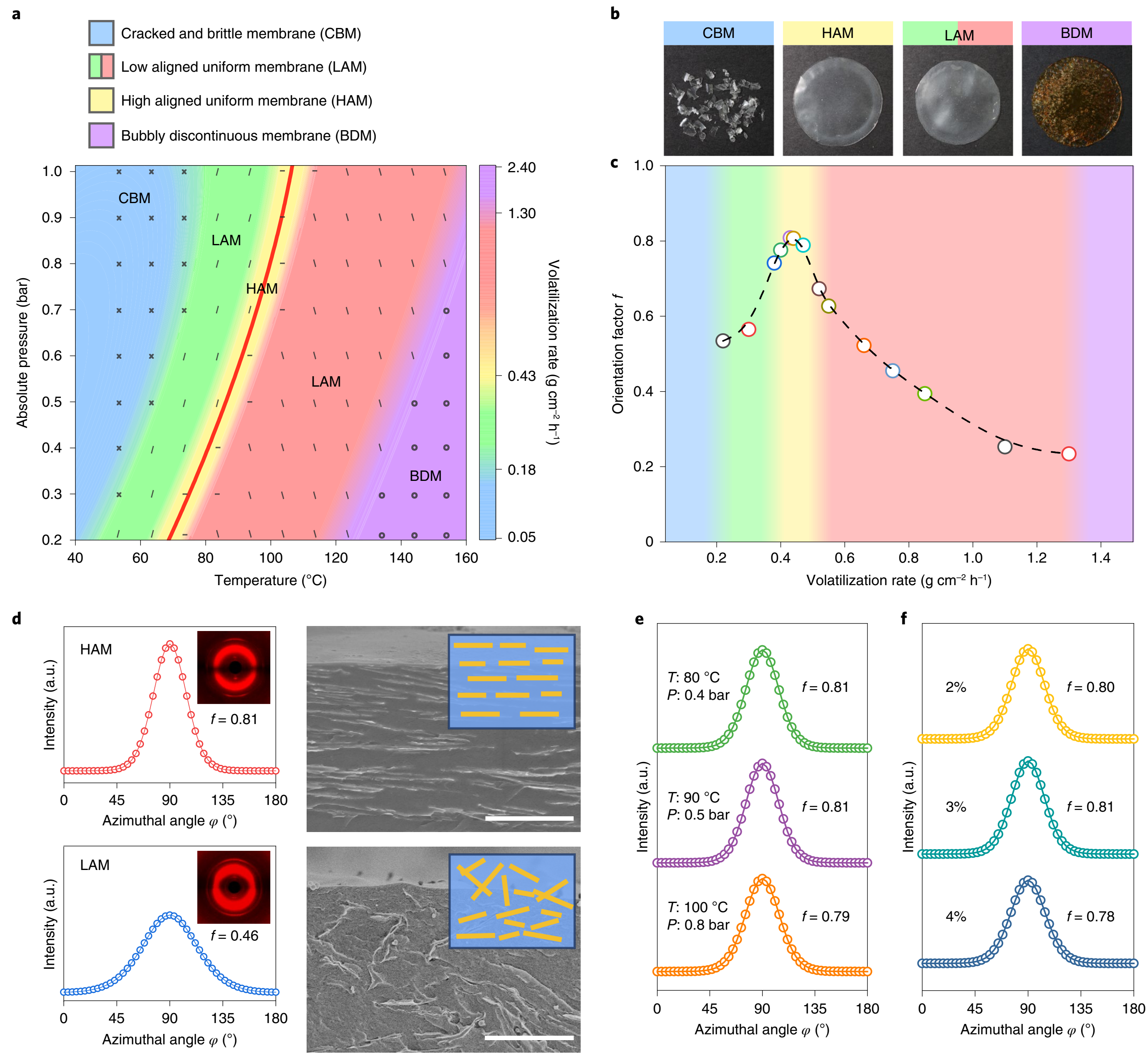

Fig. 3 | Control over the alignment of ZNs in the polymer membrane. a, The effect of volatilization rate (υ) on the membrane structure via the VSFI method, highly associated with temperature (T) and absolute pressure (P) when keeping unchanged casting solution composition. The marked points represent the experimentally tested υ at different coordinates of T and P, and the red curve represents the optimal υ for preparation of the highly aligned ZN composite membrane. **b**, Digital photographs of membranes prepared with different υ. **c**, The orientation factor (f) of membranes prepared with different υ. **d**, A typical comparison of aligned composite membranes with different f, involving cross-sectional SEM images, 2D WAXS images and azimuthal angle plots. a.u., arbitrary units. **e**,**f**, Azimuthal angle plots and the corresponding f of highly aligned ZN composite membranes prepared by keeping the optimal υ under different conditions (**e**) and highly aligned ZN composite membranes with different ZN contents prepared at optimal υ via the VSFI method (**f**). Scale bar, 5 µm (**d**).

(Supplementary Fig. 26), but also highly correlated to unique and aligned proton transport channels in aluminiferous ZNs. We performed theoretical simulations to further confirm the transport behaviour of protons in the ZNs (Fig. 4d). Compared with silicalite ZNs, protons entered aluminiferous ZNs more easily (Fig. 4e and Supplementary Fig. 27) because the ionic surface layer of aluminiferous ZN formed abundant monovalent cation-exchangeable sites (Supplementary Fig. 28), which dramatically increased their affinity for protons. However, protons exhibited faster diffusion behaviour in the hydrophobic non-ionic channel than in the ionic channel (Fig. 4f and Supplementary Fig. 29). In addition, the potential of mean force results indicated that aluminiferous ZNs have a lower energy barrier for proton transport (Supplementary Fig. 30). Therefore, we believe that the aluminiferous ZN constructs a sandwich-structured proton transport pathway with a hydrophilic ionic aluminiferous surface and hydrophobic silicalite core, realizing a rapid adsorption–diffusion–desorption process along the thickness (Fig. 4f, inset, and Supplementary Fig. 31). In contrast, the aligned silicalite ZN-based composite membrane failed to increase proton conductivity (Supplementary Figs. 32 and 33), despite showing a similar vanadium resistance ability (Supplementary Fig. 34) as the aligned aluminiferous ZN-based composite membrane.

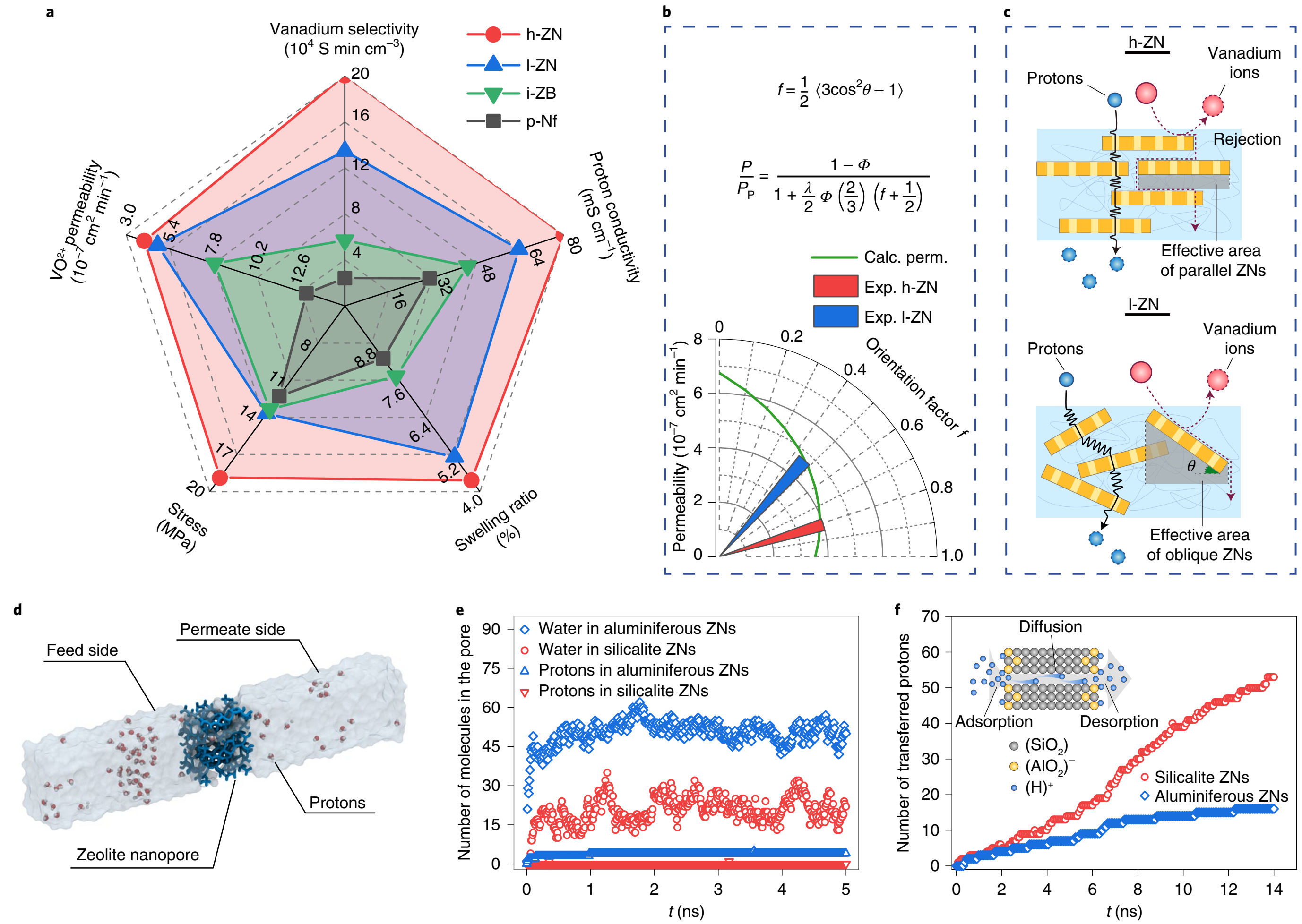

Fig. 4 | Membrane properties. a, A radar plot comparing the vanadium ion selectivity, VO^{2+} permeance, stress, proton conductivity and swelling ratio of p-Nf, h-ZN, l-ZN and i-ZB. **b**, Effect of *f* on the vanadium permeability. The calculated theoretical permeability (Calc. perm., green line) was obtained using the Bharadwaj model. Exp., experiment. **c**, Schematic of ion-selective transport processes in membranes with different *f*. **d**–**f**, Theoretical simulations of proton transport behaviours through the aligned *b* axis straight channels in ZN: schematic of the simulation system (**d**); the number of water molecules and protons entering zeolite nanopores varying with simulation time (**e**); the number of protons passing through zeolite internal channels varying with simulation time (**f**). Inset in **f** is a schematic of the fast proton adsorption–diffusion–desorption process through the aluminiferous ZN straight channel.

We also investigated the mechanical properties of the membranes. The h-ZN achieved the maximal tensile strength (Fig. 4a and Supplementary Figs. 35 and 36), indicating that the dispersion strengthening effect of aligned ZNs in the membrane was much stronger than that of disordered ZNs and bulk-type zeolite nanoparticles. The preferential orientation also enhanced the spatial confinement effect and greatly inhibited the swelling ratio of the membranes (Fig. 4a). h-ZN showed the lowest swelling ratio of 4.4%, which was approximately twice that of the pure polymeric membrane (8.3%). It is worth noting that the swelling inhibition effect did not affect the water uptake ability due to the hydrophilic porous structure of the aluminiferous zeolite (Supplementary Fig. 37).

Flow battery performance

VFB single-cell tests of these zeolite–polymer composite membranes were carried out to further assess their technological relevance (Supplementary Fig. 38). All the composite membranes exhibited better coulombic efficiency (CE), voltage efficiency (VE) and energy efficiency (EE) than the pure polymeric matrix membrane (Fig. 5a and Supplementary Fig. 39), consistent with the vanadium ion selectivity and proton conductivity results. The battery performance enhancements of the ZN composite membranes were conspicuous compared with the bulk-type zeolite composite membrane, and the excellent alignment of the ZNs in the membrane was further validated. The cell equipped with h-ZN exhibited the highest CE, VE and EE throughout the overall testing current density range (Fig. 5a and Supplementary Figs. 39 and 40). In particular, at a low current density, the CE of h-ZN apparently increased (Fig. 5b and Supplementary Fig. 39a), which is in line with the slower open-circuit voltage decay results owing to the high vanadium ion resistance (Supplementary Fig. 41). In addition, the high proton conductivity of h-ZN effectively decreased the ohmic polarization (Supplementary Fig. 42), resulting in a substantial enhancement of the VE (Fig. 5c and Supplementary Fig. 39b), as well as a higher discharge voltage and capacity (Supplementary Figs. 43 and 44). It is worth noting that the EE of h-ZN still reached 80.1% at a high current density of 200 mA cm^{-2} (Fig. 5a,c), which was more than 10% higher than that of the pure polymer membrane (69.0%). The results of the Nafion-based membranes for VFB applications are summarized in Fig. 5d and Supplementary Table 2. It is obvious that the VFB equipped with the h-ZN exhibited superior battery performance in a very wide current density range, which further identified the advantages of the alignment of ZNs in the polymer membrane.

The stability and reliability of h-ZN were further confirmed by long-term tests at a current density of 200 mA cm^{-2}. As shown in

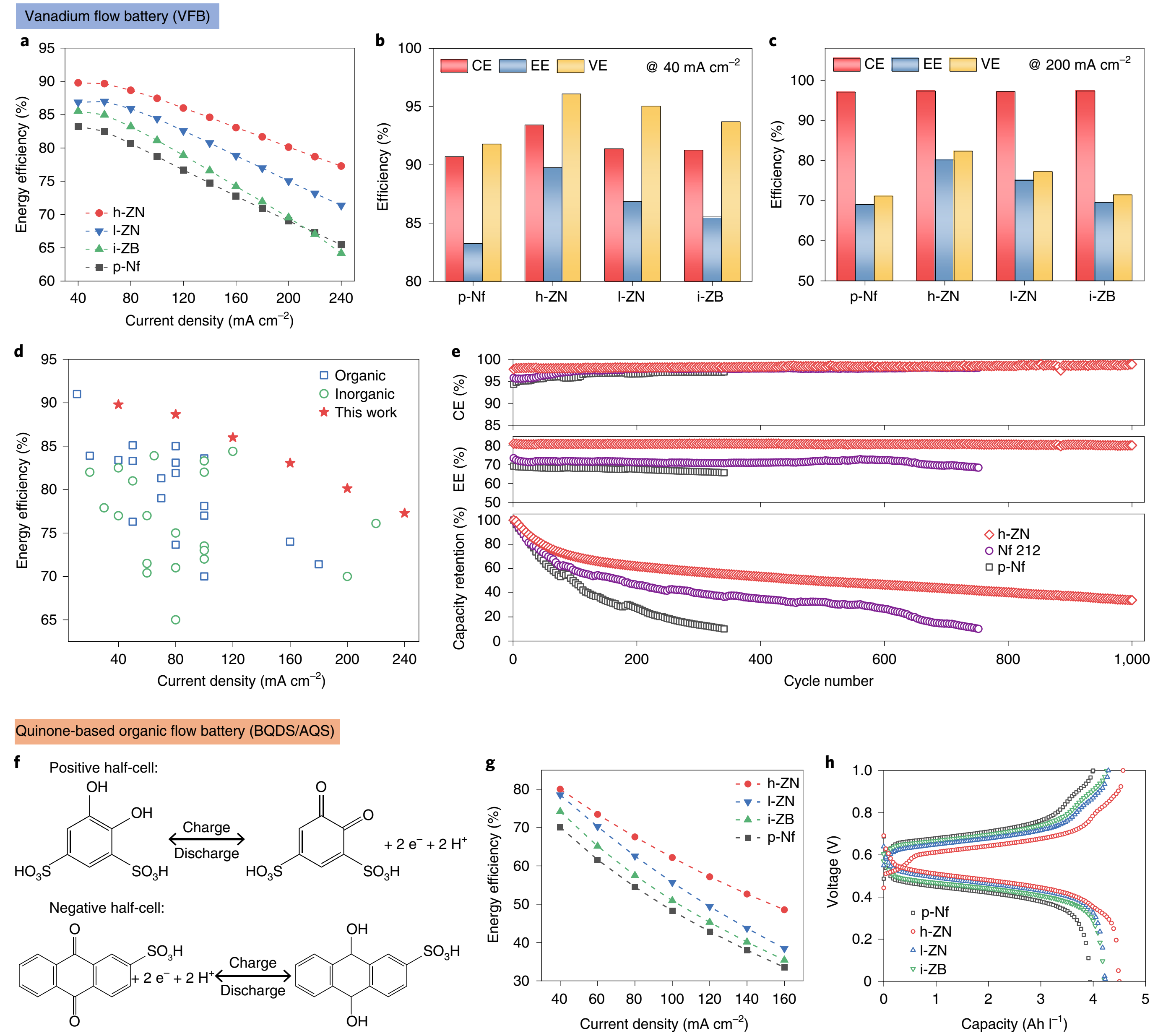

Fig. 5 | Flow battery performance. a, EE of VFB cell equipped with different membranes at the current density of 40–240 mA cm^{-2}. **b**,**c**, Battery performance comparisons of VFB cell equipped with different membranes at current densities of 40 mA cm^{-2} (**b**) and 200 mA cm^{-2} (**c**). **d**, Comparison of h-ZN with the reported Nafion-based membrane applied to VFB for EE at different current density. The organic and inorganic represent Nafion-based membranes modified by organic polymer blending and inorganic filler doping, respectively. **e**, The CE, EE and discharge capacity retention of the VFB cell equipped with different membranes for long-term tests at a current density of 200 mA cm^{-2}. Nf 212 represents commercial Nafion 212. **f**, Electrochemical reaction mechanism of a BQDS/AQS flow battery. **g**, EEs of BQDS/AQS cell equipped with different membranes at the current density of 40–160 mA cm^{-2}. **h**, Charge–discharge curves of the BQDS/AQS cell equipped with different membranes at a current density of 80 mA cm^{-2}.

Fig. 5e, the energy efficiency of the cell with h-ZN did not show an obvious decline during the entire cyclic process, maintaining ~80% after 1,000 cycles (~18 days). Benefiting from the high vanadium ion selectivity[36], h-ZN also exhibited a lower capacity decay (0.07% per cycle and 3.67% per day) than the p-Nf (0.26% per cycle and 22.61% per day) and Nf 212 (0.12% per cycle and 9.38% per day), which confirmed the stability of h-ZN in long-duration operation (Fig. 5e and Supplementary Fig. 45). In addition, h-ZN presented a stable microstructure without obvious morphological changes after 1,000 cycles (Supplementary Figs. 46 and 47). The chemical stability, especially oxidation stability, was further demonstrated by immersing a VO_2^+-containing solution for more than two weeks. There was almost no change in the absorbance spectra of the immersion solution and the weight and mechanical properties of the membranes (Supplementary Fig. 48).

Furthermore, the fast and selective ion-transport behaviour of h-ZN was further demonstrated in an aqueous quinone-based organic flow battery (Fig. 5f and Supplementary Fig. 49) with a low-cost and adjustable electrolyte[37,38], which consisted of 1,2-benzoquinone-3,5-disulfonic acid (BQDS) as the positive electrolyte and anthraquinone-2-sulfonic acid (AQS) as the negative electrolyte (labelled as BQDS/AQS). All the BQDS/AQS cells equipped with the composite membranes also exhibited enhanced CE, VE and EE compared with the p-Nf membrane (Fig. 5g and Supplementary Fig. 50), and the beneficial role of the alignment of ZNs was clear, which is consistent with the above VFB results.

For example, the BQDS/AQS cell equipped with the h-ZN demonstrated excellent battery performance with an EE of 67.2% at 80 mA cm^{-2}, which was notably higher than that with the p-Nf (EE of 55.5% at 80 mA cm^{-2}). The permeation experiments also suggested that h-ZN exhibited the strongest barrier effect on organic active species in the electrolyte (Supplementary Fig. 51 and Supplementary Table 3), and the corresponding ion selectivity of H/BQDS (Supplementary Fig. 52) reached 486.94 × 10^4 S min cm^{-3}, an order of magnitude higher than that of H/V due to a more obvious size sieving effect. At the same time, the BQDS/AQS cell equipped with h-ZN exhibited the highest discharge voltage and capacity (Fig. 5h and Supplementary Figs. 53 and 54). The stability of the h-ZN membrane in the BQDS/AQS cell was also demonstrated at a constant current density of 80 mA cm^{-2} (Supplementary Figs. 55 and 56), which retained an outstanding capacity retention of up to 95.1% after 100 charge–discharge cycles (capacity decay: ~3.5% per day).

Discussion

We demonstrate a flow-processing route to adjust the distribution and manipulate the orientation of nanosheets in a polymer matrix. The aligned ZNs maximized the efficiency of ion discrimination and proton transport. The optimized membranes effectively break the trade-off between ion selectivity and conductivity, and simultaneously exhibit superior battery performance, including in VFB and BQDS/AQS systems. The highly aligned membranes also possess higher Na$^+$ and K$^+$ conductivity, and can be well applied in other battery systems, such as a zinc–iron flow battery (Supplementary Figs. 57 and 58). The VSFI method also demonstrates the feasibility for fabrication of membranes at a larger scale (Supplementary Fig. 59). Apart from renewable energy ion separation applications, aligning high-aspect-ratio nanosheets in polymers provides an effective way to design advanced composite membranes for other fields, such as gas adsorption/separation and isomer recognition. For example, highly aligned ZNs can be realized in a polyether block amide (Pebax) polymeric matrix via the VSFI method (Supplementary Fig. 60). In addition, many opportunities derived from this align-assembled strategy will broaden the sustainable development of advanced ultrathin nanocomposite materials for water treatment and carbon capture, among others.

Methods

Materials

1,5-Diaminopentane (>97%), 1-iodopropane (99%), potassium carbonate (anhydrous, ≥99%), tetrapropylammonium hydroxide (TPAOH, 1.0 M, aqueous), sodium hydroxide (97%), potassium hydroxide (85%), silicic acid (99.9%, 20 μm), tetraethyl orthosilicate (TEOS) (98%) and 1,2-dihydroxybenzene-3,5-disulfonic acid disodium salt monohydrate (97%) were purchased from Sigma-Aldrich. Ethyl acetate (99.5%), sodium aluminate (technical), potassium chloride (99%), magnesium sulfate (99.5%) and sodium anthraquinone-2-sulfonate (97%) were purchased from Aladdin. 2-Butanone (≥99.5%), absolute ethanol (≥99.7%) and sulfuric acid (95–98%) were purchased from Yonghua Chemical. $VOSO_4$ (99%) was purchased from Nanjing Jingrui Jiuan Biotechnology. Nafion solution and Nafion 212 were purchased from Dupont. The polymer content in Nafion solution (specific gravity ~0.94) was 5 wt%, and the solvent was a mixed solvent of water, 1-propanol and ethanol with a mass ratio of 9:9:1. Pebax MH 1657 was purchased from Arkema. All chemicals were used as received, without further purification.

Synthesis of silicalite ZNs

The silicalite ZNs were bottom-up synthesized by hydrothermal growth of silicalite nano-seeds using bis-1,5(tripropyl ammonium) pentamethylene diiodide (dC5) as a structure-directing agent, as detailed in the literature[23]. In brief, the silicalite nano-seeds were synthesized from a precursor sol with a molar composition of 10 SiO_2:2.4 TPAOH:0.87 NaOH:114 H_2O by a hydrothermal reaction. The mixture was first heated at 50 °C for 6 days, then the solution was filtered with a 0.45 μm syringe filter and then the filtrate was further heated at 100 °C for 3 days. The product was washed and centrifuged to collect silicalite nano-seeds. The dC5 was synthesized by exhaustive alkylation of 1,5-diaminopentane with 1-iodopropane in the presence of potassium carbonate. The product was washed and purified using ethanol, 2-butanone and ethyl acetate, and the purity was confirmed by ^{13}C NMR. The silicalite ZNs were synthesized by secondary growth of silicalite nano-seeds in a precursor sol, which had an overall molar composition of 80 TEOS:3.75 dC5:20 KOH:9,500 H_2O. The silica molar ratio of the silicalite nano-seed suspension to the precursor sol was 1:800. The mixture was then subjected to hydrothermal reaction at 140 °C for 4 days. The as-synthesized silicalite ZNs were washed with 0.1 M KOH + 2 M KCl solution and deionized water and collected by centrifugation. The as-prepared silicalite ZNs were pretreated with piranha solution or UV/ozone several times to corrode the structure-directing agents, as previously reported[39,40]. The product was rinsed with a large amount of deionized water and dispersed in water for later use.

Synthesis of aluminiferous ZNs

The synthesis process for aluminiferous ZNs was similar to that for silicalite ZNs, as detailed in a previous report[20]. First, the precursor sol with the same molecular composition and silicalite nano-seeds was subjected to hydrothermal treatment at 140 °C for 3.5 days. Then, 1 M $NaAlO_2$ solution was added to the reaction mixture (Si/Al molar ratio of 25) to continue the hydrothermal treatment for another 0.5 day. The specific optimized process is detailed in Supplementary Note 1. The as-synthesized aluminiferous ZNs were washed with 0.1 M KOH + 2 M KCl solution and deionized water and collected by centrifugation. The as-prepared aluminiferous ZNs were pretreated as silicalite ZNs before use.

Preparation of aligned ZN Nafion composite membranes

The aligned ZN Nafion composite membrane was prepared using the VSFI alignment method. In brief, 0.79 ml of 0.5 wt% ZN suspension was mixed with 3 ml Nafion solution. Afterwards, a homogeneous suspension with 3 wt% ZN loading was obtained by stirring and ultrasonication to avoid agglomeration. The homogeneous casting solution was then poured into a flat-bottomed glass petri dish with a diameter of 41 mm (membrane size: ~13 cm^2). In the preparation of highly aligned ZN Nafion composite membranes, the solvent was volatilized at an optimal rate (0.43 ± 0.05 g cm^{-2} h^{-1}) under a certain temperature and pressure until a thin membrane was obtained. To prepare the low-aligned ZN Nafion composite membrane, the solvent was volatilized at a non-optimal rate under a certain temperature and pressure until a thin membrane was obtained. The obtained membrane was dried overnight to completely remove the solvent. After cooling to room temperature, the membrane was peeled off and immersed in deionized water for 24 h before use. A pure Nafion membrane without zeolite was prepared using the same procedure.

Preparation of Nafion composite membrane with bulk-type zeolite

The bulk-type zeolite was synthesized by hydrothermal crystallization using a precursor sol of 25 TEOS:3.3 TPAOH:1,120 H_2O:$NaAlO_2$. Typically, the precursor solution was obtained by mixing 11.3 ml TPAOH, 19.2 ml TEOS, 60 ml deionized water and 0.28 g $NaAlO_2$. The precursor solution was hydrolysed overnight at room temperature and then filtered with a 0.45 μm syringe filter. Hydrothermal synthesis was conducted at 180 °C for 4 h. The as-synthesized bulk-type zeolite was rinsed with deionized water, dried and calcined to remove the structure-directing agents before use. Bulk-type zeolite (3.9 mg) was added to a 3 ml Nafion solution (3 wt% zeolite loading), followed by vigorous stirring and ultrasonication. The preparation procedure for the membrane with bulk-type zeolite was the same as that for the highly aligned ZN Nafion composite membrane.

Preparation of aligned ZN Pebax membrane

The 2 wt% Pebax solution was obtained by adding Pebax to a mixed solvent with ethanol and water (w_{ethanol}:w_{water} = 7:3) followed by stirring at 80 °C for 2 h. A 0.79 ml portion of the 0.5 wt% ZN suspension was added to a 6.5 ml as-prepared Pebax solution (3 wt% nanosheet loading), followed by vigorous stirring and ultrasonication. The preparation procedure for the Pebax membrane with aligned ZN was the same as that for the Nafion membrane with aligned ZN. A pure Pebax membrane without a zeolite nanosheet was prepared using the same procedure.

Characterization

SEM and EDS were performed using a Hitachi S-4800 microscope equipped with an energy dispersive X-ray detector. For the membrane cross-section examination, the membrane was immersed in liquid nitrogen and then fractured with tweezers. The samples were coated with gold prior to SEM analysis. The cross-sectional membrane sample for TEM was sliced with a Leica EM UC7-FC7 and then characterized using an FEI Tecnai G2 F20. ^{13}C NMR liquid spectra were collected on a Bruker ACF-400. Atomic force microscopy images were obtained using a Park XE-100. Cs-corrected integrated differential phase contrast scanning transmission electron microscopy images were taken at 300 kV on an FEI Titan Cubed Themis G2 300 scanning transmission electron microscope. The quantitative elemental composition of the zeolite nanosheets was analysed by X-ray photoelectron spectroscopy (Shimadzu Kratos AXIS Supra). The thermal stability of the ZNs was measured by thermogravimetric analysis (Netzsch STA 449 F3) by heating the samples from 25 to 700 °C in air. The mechanical properties of the membranes were tested using a tensile tester (XQ-1C, Shanghai New Fiber Instrument) at room temperature by tailoring the membrane samples to a width of 2 mm and a length of 10 mm, and all the membranes were exposed to ambient temperature and humidity before tests. The tensile rate was fixed at 10 mm min^{-1}. The crystal structure of the zeolite was characterized by X-ray diffraction (Rigaku Miniflex 600). WAXS characterization was performed using a Xeuss 2.0. N_2 sorption–desorption isotherms of ZNs at 77 K were determined using a Micromeritics ASAP2460 instrument.

Other characterizations and properties measured for the membranes, including water uptake, swelling ratio, oxidation stability test, vanadium ion permeability, area resistance, conductivity, ion selectivity, positron annihilation lifetime spectroscopy and FIB-SEM tomography, are detailed in the Supplementary Information.

Estimation of the orientation order parameter *f*

Herman's orientation factor *f* was calculated using the azimuthal angle plots obtained from the 2D WAXS images using equations (1) and (2)[41]. The *f* values range between 0 and 1, where the former corresponds to an isotropic structure, and the latter corresponds to perfect orientation along the director.

$$f = \frac{3\langle\cos^2\varphi\rangle - 1}{2} \tag{1}$$

and

$$\langle\cos^2\varphi\rangle = \frac{\int_0^{\frac{\pi}{2}} I(\varphi)\ \cos^2\varphi\ \sin\varphi\ \mathrm{d}\varphi}{\int_0^{\frac{\pi}{2}} I(\varphi)\sin\varphi\ \mathrm{d}\varphi}\varphi \tag{2}$$

where φ is the azimuthal angle and $I(\varphi)$ is the intensity distribution function with azimuthal angle φ. $\langle\cos^2\varphi\rangle$ was calculated by integrating the intensity of the specific 2θ diffraction peak along φ.

Calculation of permeability based on Bharadwaj model

To understand the effect of the orientation degree on vanadium ion permeability, we calculated the theoretical permeability based on the Bharadwaj model[33]. In brief, the integration of impermeable layered ZNs into a polymeric matrix introduces a tortuous diffusive path for vanadium ions, which in turn leads to a decrease in permeability. The effect of tortuosity on the permeability can be expressed as in equation (3).

$$\frac{P}{P_{\text{p}}} = \frac{1-\Phi}{\tau} \tag{3}$$

where P and P_{p} are the permeabilities of the membranes with ZNs and p-Nf membranes, respectively. Φ is the volume fraction of ZNs. τ is the tortuosity factor defined as the ratio of the actual distance (d') that vanadium ions must travel to the shortest distance (d) that it would have travelled in the absence of ZNs. τ can be expressed using equation (4), when it is assumed that the normal of all ZNs is consistent with the direction of diffusion.

$$\tau = \frac{d'}{d} = 1 + \frac{\lambda}{2}\Phi \tag{4}$$

where λ is the aspect ratio of ZNs.

However, the arrangement of ZNs is often random, and the orientation of the arrangement can be expressed by the orientation factor *f*:

$$f = \frac{1}{2}\langle 3\cos^2\theta - 1\rangle \tag{5}$$

where θ is the angle between the normal of the ZN and the membrane surface normal. The angular brackets denote the average of all the ZNs in the membrane.

Considering that any deviation of the ZN arrangement will actually affect the barrier effect of vanadium ions, the tortuosity factor can be modified as

$$\tau = 1 + \frac{\lambda}{2}\Phi\langle\cos^2\theta\rangle = 1 + \frac{\lambda}{2}\Phi\left(\frac{2}{3}\right)\left(f + \frac{1}{2}\right) \tag{6}$$

As a result, equation (3) can be expressed as:

$$\frac{P}{P_{\text{p}}} = \frac{1-\Phi}{1 + \frac{\lambda}{2}\Phi(\frac{2}{3})(f + \frac{1}{2})} \tag{7}$$

Computational fluid dynamics

The COMSOL Multiphysics software was used to simulate the angle-adjustment process of the ZN. The liquid phase is described by a laminar flow model:

$$\rho_{\text{l}}\frac{\partial u_{\text{l}}}{\partial t} + \rho_{\text{l}}(u_{\text{l}}\nabla)u_{\text{l}} = \nabla[-pI + K] + F + \rho_{\text{l}}g \tag{8}$$

$$\rho_l \nabla u_l = 0 \tag{9}$$

where u_{l} is the velocity of the liquid, p is the static pressure, I is the identity diagonal matrix, K is the viscous stress tensor, F is the external force term, ρ_l is the density of the liquid and g is the gravitational acceleration.

The ZN is described by solid mechanics:

$$\rho_s\frac{\partial^2 u_{\text{s}}}{\partial t^2} = \nabla(FS)^T + F_{\text{v}} \tag{10}$$

$$F = I + \nabla u_{\text{s}} \tag{11}$$

where ρ_{s} is the density of ZN, S is the strain-rate tensor, and F_{v} is the volumetric load. ZN is set to a length and width of 10 nm × 0.1 nm rigid rectangle. In this system, ZN is subjected to gravity, buoyancy from the solvent and shear force simultaneously. With the simulation, the orientation of the ZN changes and the angle to the horizontal gradually decreases. To describe the change in the ZN position and orientation, a moving grid was used to regenerate the grid according to the change in geometry after each simulation.

Molecular dynamics simulation

The atomistic structure of the MFI-type zeolite nanosheet was obtained from the International Zeolite Association database. The aluminiferous zeolite structure was constructed by applying Lowenstein's rule (Al–O–Al linkages are not allowed) with a Si/Al molar ratio of 25. All dangling bonds of the silicon atoms on both zeolite surfaces were saturated with –OH groups. The nanosheet was modelled as a zeolite fragment with a thickness of ~22 Å. The model was then moved into a simulation cell with two water reservoirs placed on both sides. 4 M Hydronium ions and 2 M sulfate ions were added to the water reservoir on the left side while keeping pure water on the right side.

All simulations were performed using the large-scale atomic/molecular massively parallel simulator package[42]. The interactions of all atoms were described by the 12-6 Lennard-Jones (LJ) and Coulombic potentials. The SPC/E solvation model[43] was used for water molecules. To decrease the high-frequency vibrations to reduce the simulation time, the bonds and angles of the water molecules were constrained by the SHAKE algorithm. The force-field parameters for the zeolite membranes were taken from Emami et al.[44], which were previously validated against experimental data. A small, stable hydrated proton (that is, H_3O^+) was used to describe the excess protons in the aqueous solutions[45] and the force-field parameters for SO_4^{2-} were obtained from a previous report[46]. The particle–particle particle–mesh algorithm with a root mean square accuracy of 10^{-5} was used to compute the long-range electrostatic interactions. The cutoff distances for short-range LJ and Coulombic potential were both set to 1.0 nm.

Each system was initially subjected to energy minimization, with a tolerance of 10^{-5}. The temperature was set at 300 K for all simulations. A time step of 1 fs was employed. The periodic boundary conditions (PBC) were applied in the x and y directions during the process of free diffusion, where hydronium ions were driven by the concentration difference between the two sides. To simulate the directional transport behaviours of the hydronium ions, an electric field with intensity of 0.05 V $Å^{-1}$ was applied along the z direction to generate the effective transmembrane voltage. In this case, PBC was applied in all directions, and each production run was first equilibrated for 5 ns and at 15 ns minimum for data analysis.

Battery performance

A home-made VFB single cell was assembled by sandwiching the membrane between two carbon felt electrodes with an effective area of 4 cm^2 (2 cm × 2 cm) and clamped by two graphite plates. A 10 ml portion of 1.5 M V^{2+}/V^{3+} in 3 M H_2SO_4 and 10 ml of 1.5 M VO^{2+}/VO_2^+ in 3 M H_2SO_4 were used as the negative and positive electrolytes, respectively. The electrolytes were cyclically pumped through the corresponding electrodes. A Neware CT-4008 was used to test the charge–discharge performance over a voltage range of 0.8–1.7 V at various current densities. A long-term test was conducted at 200 mA cm^{-2}, and the test was terminated when the discharge capacity retention decreased to 10%. Open-circuit voltage decay (0.8 V lower limit voltage) was tested at 50% state of charge, and the cell polarization was examined at ~100% state of charge. All membranes were activated by repeating the charge–discharge process for several cycles before testing.

The performance of the aqueous quinone-based organic flow battery was the same as that of the VFB system. 1,2-Dihydroxybenzene-3,5-disulfonic acid disodium salt and anthraquinone-2-disulfonic acid sodium salts were subjected to ion exchange to obtain their acid form with increased solubility in aqueous solutions, as previously reported[37]. The resulting solutions consisting of 0.2 M 1,2-dihydroxybenzene-3,5-disulfonic acid (charged form was BQDS) in 1 M H_2SO_4 (10 ml) and 0.2 M AQS in 1 M H_2SO_4 (10 ml) were used as the positive and negative electrolytes of the aqueous quinone-based organic cell, respectively. The charge and discharge cutoff voltages were set to 1 V and 0.01 V, respectively. All membranes were activated by repeating the charge–discharge process for several cycles before testing.

In zinc–iron flow battery tests, 10 ml of 0.6 M $K_4Fe(CN)_6$ in 5 M NaOH and 10 ml of 0.3 M $Zn(OH)_4^{2-}$ in 5 M NaOH were used as positive and negative electrolytes, respectively. The charge process was controlled by the charging time to maintain a constant charge capacity, while the discharging process was terminated by setting a cutoff voltage of 0.1 V.

The efficiencies of single cells were evaluated using the CE, VE and EE, and were calculated using equations (12), (13) and (14):

$$\mathrm{CE}=\frac{Q_{\mathrm{discharge}}}{Q_{\mathrm{charge}}}\times 100\% \tag{12}$$

$$\mathrm{EE}=\frac{E_{\mathrm{discharge}}}{E_{\mathrm{charge}}}\times 100\% \tag{13}$$

$$\mathrm{VE}=\frac{\mathrm{EE}}{\mathrm{CE}}\times 100\% \tag{14}$$

where $Q_{\mathrm{discharge}}$ and Q_{charge} are the discharge capacity and charge capacity per charge–discharge cycle, and $E_{\mathrm{discharge}}$ and E_{charge} are discharge energy and charge energy per charge–discharge cycle.

Reporting summary

Further information on research design is available in the Nature Research Reporting Summary linked to this article.

Data availability

All data generated and/or analysed in this study are included in this published article and its Supplementary Information file. The data that support the findings of this study are available from the corresponding author upon reasonable request.

References

1. Dai, Q. et al. Thin-film composite membrane breaking the trade-off between conductivity and selectivity for a flow battery. *Nat. Commun.* **11**, 13 (2020).
2. Li, Z. & Lu, Y.-C. Polysulfide-based redox flow batteries with long life and low levelized cost enabled by charge-reinforced ion-selective membranes. *Nat. Energy* **6**, 517–528 (2021).
3. Zhang, D. et al. Advanced Nafion hybrid membranes with fast proton transport channels toward high-performance vanadium redox flow battery. *J. Membr. Sci.* **624**, 119047 (2021).
4. Jiao, K. et al. Designing the next generation of proton-exchange membrane fuel cells. *Nature* **595**, 361–369 (2021).
5. He, G. et al. Nanostructured ion-exchange membranes for fuel cells: recent advances and perspectives. *Adv. Mater.* **27**, 5280–5295 (2015).
6. Lindquist, G. A., Xu, Q., Oener, S. Z. & Boettcher, S. W. Membrane electrolyzers for impure-water splitting. *Joule* **4**, 2549–2561 (2020).
7. Chen, P. & Hu, X. High-efficiency anion exchange membrane water electrolysis employing non-noble metal catalysts. *Adv. Energy Mater.* **10**, 2002285 (2020).
8. Lu, W. et al. Porous membranes in secondary battery technologies. *Chem. Soc. Rev.* **46**, 2199–2236 (2017).

9. Ye, J. et al. Hybrid membranes dispersed with superhydrophilic TiO_2 nanotubes toward ultra-stable and high-performance vanadium redox flow batteries. *Adv. Energy Mater.* **10**, 1904041 (2020).
10. Zuo, P. et al. Sulfonated microporous polymer membranes with fast and selective ion transport for electrochemical energy conversion and storage. *Angew. Chem. Int. Ed. Engl.* **59**, 9564–9573 (2020).
11. Dai, L., Huang, K., Xia, Y. & Xu, Z. Two-dimensional material separation membranes for renewable energy purification, storage, and conversion. *Green Energy Environ.* **6**, 193–211 (2021).
12. Tan, R. et al. Hydrophilic microporous membranes for selective ion separation and flow-battery energy storage. *Nat. Mater.* **19**, 195–202 (2020).
13. Lu, Z., Wu, Y., Ding, L., Wei, Y. & Wang, H. A lamellar MXene ($Ti_3C_2T_x$)/PSS composite membrane for fast and selective lithium-ion separation. *Angew. Chem. Int. Ed. Engl.* **60**, 22265–22269 (2021).
14. Sheng, F. et al. Efficient ion sieving in covalent organic framework membranes with sub-2-nanometer channels. *Adv. Mater.* **33**, 2104404 (2021).
15. Ding, L. et al. Effective ion sieving with $Ti_3C_2T_x$ MXene membranes for production of drinking water from seawater. *Nat. Sustain.* **3**, 296–302 (2020).
16. Dai, L. et al. Ultrafast water transport in two-dimensional channels enabled by spherical polyelectrolyte brushes with controllable flexibility. *Angew. Chem. Int. Ed. Engl.* **60**, 19933–19941 (2021).
17. Liu, X. et al. Magnetic field alignment of stable proton-conducting channels in an electrolyte membrane. *Nat. Commun.* **10**, 842 (2019).
18. Zhang, D. et al. Oriented proton-conductive nanochannels boosting a highly conductive proton-exchange membrane for a vanadium redox flow battery. *ACS Appl. Mater. Interfaces* **13**, 4051–4061 (2021).
19. Rangnekar, N., Mittal, N., Elyassi, B., Caro, J. & Tsapatsis, M. Zeolite membranes – a review and comparison with MOFs. *Chem. Soc. Rev.* **44**, 7128–7154 (2015).
20. Cao, Z. et al. Ultrathin ZSM-5 zeolite nanosheet laminated membrane for high-flux desalination of concentrated brines. *Sci. Adv.* **4**, eaau8634 (2018).
21. Min, B. et al. Continuous zeolite MFI membranes fabricated from 2D MFI nanosheets on ceramic hollow fibers. *Angew. Chem. Int. Ed. Engl.* **58**, 8201–8205 (2019).
22. Kim, D., Jeon, M. Y., Stottrup, B. L. & Tsapatsis, M. *para*-Xylene ultra-selective zeolite MFI membranes fabricated from nanosheet monolayers at the air–water interface. *Angew. Chem. Int. Ed. Engl.* **57**, 480–485 (2018).
23. Jeon, M. Y. et al. Ultra-selective high-flux membranes from directly synthesized zeolite nanosheets. *Nature* **543**, 690–694 (2017).
24. Park, H. B., Kamcev, J., Robeson, L. M., Elimelech, M. & Freeman, B. D. Maximizing the right stuff: the trade-off between membrane permeability and selectivity. *Science* **356**, eaab0530 (2017).
25. Liu, G. et al. Mixed matrix formulations with MOF molecular sieving for key energy-intensive separations. *Nat. Mater.* **17**, 283–289 (2018).
26. Zhang, Q., Zhou, M., Liu, X. & Zhang, B. Pebax/two-dimensional MFI nanosheets mixed-matrix membranes for enhanced CO_2 separation. *J. Membr. Sci.* **636**, 119612 (2021).
27. Yuan, Z. et al. A highly ion-selective zeolite flake layer on porous membranes for flow battery applications. *Angew. Chem. Int. Ed. Engl.* **55**, 3058–3062 (2016).
28. Wang, S. et al. Two-dimensional nanochannel membranes for molecular and ionic separations. *Chem. Soc. Rev.* **49**, 1071–1089 (2020).
29. Rodenas, T. et al. Metal–organic framework nanosheets in polymer composite materials for gas separation. *Nat. Mater.* **14**, 48–55 (2015).
30. Guell, D. & Bénard, A. in *Flow-Induced Alignment in Composite Materials* (eds Papathanasiou, T.D. & Guell, D.C.) 1–42 (Woodhead Publishing, 1997).
31. Ding, F. et al. Biomimetic nanocoatings with exceptional mechanical, barrier, and flame-retardant properties from large-scale one-step coassembly. *Sci. Adv.* **3**, e1701212 (2017).
32. Zhao, C. et al. Layered nanocomposites by shear-flow-induced alignment of nanosheets. *Nature* **580**, 210–215 (2020).
33. Bharadwaj, R. K. Modeling the barrier properties of polymer-layered silicate nanocomposites. *Macromolecules* **34**, 9189–9192 (2001).
34. Kusoglu, A. & Weber, A. Z. New insights into perfluorinated sulfonic-acid ionomers. *Chem. Rev.* **117**, 987–1104 (2017).
35. Ling, X., Bonn, M., Parekh, S. H. & Domke, K. F. Nanoscale distribution of sulfonic acid groups determines structure and binding of water in Nafion membranes. *Angew. Chem. Int. Ed. Engl.* **55**, 4011–4015 (2016).
36. Yao, Y., Lei, J., Shi, Y., Ai, F. & Lu, Y.-C. Assessment methods and performance metrics for redox flow batteries. *Nat. Energy* **6**, 582–588 (2021).
37. Zhang, L., Zhang, S., Li, E., Zhao, L. & Zhang, S. Sulfonated poly(ether ether ketone) membrane for quinone-based organic flow batteries. *J. Membr. Sci.* **584**, 246–253 (2019).
38. Winsberg, J., Hagemann, T., Janoschka, T., Hager, M. D. & Schubert, U. S. Redox-flow batteries: from metals to organic redox-active materials. *Angew. Chem. Int. Ed. Engl.* **56**, 686–711 (2017).
39. Zhang, H. et al. Open-pore two-dimensional MFI zeolite nanosheets for the fabrication of hydrocarbon-isomer-selective membranes on porous polymer supports. *Angew. Chem. Int. Ed. Engl.* **55**, 7184–7187 (2016).
40. Yang, S. et al. Highly selective SSZ-13 zeolite hollow fiber membranes by ultraviolet activation at near-ambient temperature. *ChemNanoMat* **5**, 61–67 (2019).
41. Ye, D. et al. Ultrahigh tough, super clear, and highly anisotropic nanofiber-structured regenerated cellulose films. *ACS Nano* **13**, 4843–4853 (2019).
42. Plimpton, S. Fast parallel algorithms for short-range molecular dynamics. *J. Comput. Phys.* **117**, 1–19 (1995).
43. Berendsen, H. J. C., Grigera, J. R. & Straatsma, T. P. The missing term in effective pair potentials. *J. Phys. Chem.* **91**, 6269–6271 (1987).
44. Emami, F. S. et al. Force field and a surface model database for silica to simulate interfacial properties in atomic resolution. *Chem. Mater.* **26**, 2647–2658 (2014).
45. Jang, S. S., Molinero, V., Çağın, T. & Goddard, W. A. Nanophase-segregation and transport in Nafion 117 from molecular dynamics simulations: effect of monomeric sequence. *J. Phys. Chem. B* **108**, 3149–3157 (2004).
46. Williams, C. D. & Carbone, P. A classical force field for tetrahedral oxyanions developed using hydration properties: the examples of pertechnetate (TcO_4^-) and sulfate (SO_4^{2-}). *J. Chem. Phys.* **143**, 174502 (2015).

Acknowledgements

This work is supported by National Key Research and Development Program of China (grant no. 2021YFB3801301), National Natural Science Foundation of China (grant nos. 22278211, 22075076 and

21908054) and Priority Academic Program Development of Jiangsu Higher Education Institutions (PAPD).

Author contributions

Yongsheng Xia, K.H. and Z.X. conceived the idea and designed the experiments. K.H., W.X., W.J. and Z.X. supervised the project. Yongsheng Xia conducted the experiments and data analysis. H.C. helped with some of the battery performance tests. Y.C. and C.L. contributed to the computational fluid dynamics simulation. F.X. contributed to the MD simulation. Yu Xia and D.Z. helped with some of the material synthesis. L.D. and K.Q. helped with some of the characterizations. Yongsheng Xia and K.H. organized and wrote the manuscript. All authors contributed to the discussion and revision of the manuscript.

Competing interests

The authors declare no competing interests.

Additional information

Supplementary information The online version contains supplementary material available at https://doi.org/10.1038/s41893-022-00974-w.

Correspondence and requests for materials should be addressed to Kang Huang, Wanqin Jin or Zhi Xu.

Peer review information *Nature Sustainability* thanks Yi-Chun Lu and the other, anonymous, reviewer(s) for their contribution to the peer review of this work.

nature research

Corresponding author(s): Zhi Xu, Wanqin Jin, Kang Huang

Last updated by author(s): Jul 18, 2022

Reporting Summary

Nature Research wishes to improve the reproducibility of the work that we publish. This form provides structure for consistency and transparency in reporting. For further information on Nature Research policies, see our Editorial Policies and the Editorial Policy Checklist.

Statistics

For all statistical analyses, confirm that the following items are present in the figure legend, table legend, main text, or Methods section.

n/a	Confirmed	
☐	☒	The exact sample size (n) for each experimental group/condition, given as a discrete number and unit of measurement
☐	☒	A statement on whether measurements were taken from distinct samples or whether the same sample was measured repeatedly
☒	☐	The statistical test(s) used AND whether they are one- or two-sided *Only common tests should be described solely by name; describe more complex techniques in the Methods section.*
☒	☐	A description of all covariates tested
☒	☐	A description of any assumptions or corrections, such as tests of normality and adjustment for multiple comparisons
☐	☒	A full description of the statistical parameters including central tendency (e.g. means) or other basic estimates (e.g. regression coefficient) AND variation (e.g. standard deviation) or associated estimates of uncertainty (e.g. confidence intervals)
☒	☐	For null hypothesis testing, the test statistic (e.g. F, t, r) with confidence intervals, effect sizes, degrees of freedom and P value noted *Give P values as exact values whenever suitable.*
☒	☐	For Bayesian analysis, information on the choice of priors and Markov chain Monte Carlo settings
☒	☐	For hierarchical and complex designs, identification of the appropriate level for tests and full reporting of outcomes
☒	☐	Estimates of effect sizes (e.g. Cohen's d, Pearson's r), indicating how they were calculated

Our web collection on statistics for biologists contains articles on many of the points above.

Software and code

Policy information about availability of computer code

Data collection	COMSOL Multiphysics 5.6 was used to perform computational fluid dynamics, and LAMMPS 3Mar20 was used to perform molecular dynamics simulation.
Data analysis	Origin 2021 and Matlab R2014a for data analysis and data fitting.

For manuscripts utilizing custom algorithms or software that are central to the research but not yet described in published literature, software must be made available to editors and reviewers. We strongly encourage code deposition in a community repository (e.g. GitHub). See the Nature Research guidelines for submitting code & software for further information.

Data

Policy information about availability of data

All manuscripts must include a data availability statement. This statement should provide the following information, where applicable:

- Accession codes, unique identifiers, or web links for publicly available datasets
- A list of figures that have associated raw data
- A description of any restrictions on data availability

All data generated or analyzed during this study are included in this published article and its supplementary information files.

Field-specific reporting

Please select the one below that is the best fit for your research. If you are not sure, read the appropriate sections before making your selection.

☒ Life sciences ☐ Behavioural & social sciences ☐ Ecological, evolutionary & environmental sciences

For a reference copy of the document with all sections, see nature.com/documents/nr-reporting-summary-flat.pdf

Life sciences study design

All studies must disclose on these points even when the disclosure is negative.

Sample size	At least three membrane samples for each experiment in this study were prepared for parallel experiments to verify the reproducibility of the experimental finding.
Data exclusions	No data were excluded from the analyses.
Replication	At least three membrane samples for each experiment in this study were prepared for parallel experiments to verify the reproducibility of the experimental finding, and all attempts at replication were successful.
Randomization	All samples in this study were randomly allocated into experimental groups.
Blinding	The investigators were blinded to group allocation during data collection and/or analysis.

Reporting for specific materials, systems and methods

We require information from authors about some types of materials, experimental systems and methods used in many studies. Here, indicate whether each material, system or method listed is relevant to your study. If you are not sure if a list item applies to your research, read the appropriate section before selecting a response.

Materials & experimental systems

n/a	Involved in the study
☒	☐ Antibodies
☒	☐ Eukaryotic cell lines
☒	☐ Palaeontology and archaeology
☒	☐ Animals and other organisms
☒	☐ Human research participants
☒	☐ Clinical data
☒	☐ Dual use research of concern

Methods

n/a	Involved in the study
☒	☐ ChIP-seq
☒	☐ Flow cytometry
☒	☐ MRI-based neuroimaging